Flow pattern of non-Newtonian fluids in reciprocating scraped surface heat exchangers

D. Crespí-Llorens [a,*], P. Vicente [a], A. Viedma [b]

[a] Dep. Ing. Mecánica y Energía, Universidad Miguel Hernández, Av. Universidad, s/n, 03202 Elche, Spain
[b] Dep. Ing. Térmica y de Fluidos, Universidad Politécnica de Cartagena, Dr. Fleming, s/n, 30202 Cartagena, Spain

ABSTRACT

The flow pattern of a pseudoplastic fluid inside a scraped surface heat exchanger has been obtained by means of Particle Image Velocimetry. The scraping device consists of a rod with semicircular pieces mounted on it, which are in contact with the inner surface of the pipe. The whole moves axially and thus the pieces scrape the inner surface of the pipe, in order to avoid fouling formation and enhance heat transfer.

The aim of this work is to obtain the influence on the flow pattern of the significant parameters of the problem: the Reynolds number, the scraping velocity and the non-Newtonian behaviour of the fluid. In order to achieve this, a numerical model has been created. This model provides the velocity profile of non-Newtonian fluids in a concentric annulus, which has been used as start point for the study of the flow in the pipe with the insert device. Finally, PIV experiments have been carried out in the geometry under study, covering the representative ranges of the mentioned variables.

The results provide a deeper knowledge of the flow, allowing for a better understanding of the flow structures, as well as of the consequences they can have on linear pressure drop and heat transfer and on their study. Furthermore, the possibility of applying a suitable generalization method for the viscosity in this device has been analysed.

© 2016 Elsevier Inc. All rights reserved.

1. Introduction

Many fluids in the food and chemical or petrochemical industries are non-Newtonian. An important characteristic of these fluids is that they have large apparent viscosities; therefore, laminar flow conditions occur more often than with Newtonian fluids and Prandtl numbers are high.

The fouling problem in heat exchangers has a significant impact on these industries and can be even more important in processes involving non-Newtonian fluids [5]. Preventing fouling on heat exchanging devices is essential to avoid heat transfer inefficiencies, cleaning downtime, health risk, corrosion due to deposit formation and pressure loss, which affects the devices' performance and energy consumption [3–5]. Besides, heat transfer to viscous non-Newtonian flows is usually inefficient and produces significant temperature differences in the fluid, which can yield to low quality products, especially in the food industry.

Insert devices have been deeply investigated [21] in order to improve their efficiency: heat transfer vs. pressure drop. Heat transfer enhancement techniques can be classified into *active* and *passive*. The *passive* ones, like inserted wire coils or mechanically deformed pipes, have been studied for the last 30 years and have become commercial solutions. Webb deduced from his work that *active* techniques can produce very high increases in heat transfer, especially in laminar flow.

Mechanically assisted heat exchangers, where a heat transfer surface is periodically scraped by a moving element, might be used to increase heat transfer and avoid fouling. Many investigations have focused on these anti-fouling devices, studying flow pattern characteristics [20], their thermo-hydraulic performance [11] or scraping efficiency [19].

This work presents a study of the flow pattern in a scraped surface heat exchanger using a pseudoplastic non-Newtonian fluid, which is the most common non-Newtonian behaviour in the process industry [8,7]. For them, in a certain range of shear stress, the viscosity decreases as shear stress increases. In this research, the *Power Law* model will be used to explain the rheology of the fluid. The pipe heat exchanger under study has an inserted active device, which is especially designed to avoid fouling. Additionally, the design of the insert device produces mass transfer between core and peripheral regions of the flow, which leads to heat

* Corresponding author.
   E-mail address: dcrespi@umh.es (D. Crespí-Llorens).

Nomenclature

D, R	inner diameter and radius of the acrylic pipe (see Fig. 1) [m]
d, R_s	diameter and radius of the insert device rod (see Fig. 1) [m]
D_h	hydraulic diameter (see Fig. 1) [m]
L	longitudinal position referenced to the centre of the scraper, being positive downstream of it [mm]
N	number of pair of images in an experiment
NN	number of finite volumes of the mesh
m	flow consistency index (rheological property) [Pa s^n]
Q	flow rate [m^3/s]
P	distance from one scraper to the next one at the same angular position [m]
p	pressure [Pa]
r	radial position [m]
s	standard deviation or Root Mean Square function (RMS)
t	scraper length (see Fig. 1) [mm]
T	temperature [°C]
u	fluid velocity [m/s]
u_b	bulk velocity [m/s]
u_i, U_i	instant and average velocities of the fluid at a point of the flow field [m/s]
v_s	velocity of the scraper [m/s]
$Z1, Z2, Z3$	regions of the flow fields. Depicted in Fig. 7
S_A, S_B	refer to sections located at $z = (P - t)/2$ and $z = 3(P - t)/4$ downstream of the scraper

r, z	radial and axial coordinates

Dimensionless number

a, b	constants of the Generalized Reynolds number definition (see Table 1)
β	blockage parameter, $\beta = 1 - v_s/u_b$
r^*	non dimensional radial position, $r^* = 2r/(D - d)$
Re_b	Reynolds number, $Re_b = \rho u_b^{2-n} D_h^n/m$
Re_g	Generalized Reynolds number defined by Crespí-Llorens et al. [10] for the geometry under study (pipe with insert device), $Re_g = Re_b/(a^{n-1}n^b)$
ω	non-dimensional scraping velocity, $\omega = v_s/u_b = 1 - \beta$

Greek symbols

α	aspect ratio $\alpha = d/D$ [Pa]
τ	shear stress [Pa]
μ	dynamic viscosity of the fluid for the numerical model (see Eq. (10)) [Pa s]
ρ	density of the fluid [kg/m^3]

Subscripts

s	scraper
N, S, W, E	refer to North, South, West or East surface of a finite volume (see Fig. 5(b))

transfer enhancements [18] and uniform fluid temperatures in highly viscous flows. The insert device consists of a rod with semi-circle shaped scrapers mounted on it, as shown in Fig. 1. The whole is impelled alternatively along the axial direction by a hydraulic cylinder. Solano et al. [16,17] studied this device using Newtonian fluids and obtained the flow structures in different conditions and Boodhoo et al. [6] studied the same device working with a gas–solid mixture. Consequently, this paper is focused on evaluating the impact of using a non-Newtonian working fluid. For that, the flow pattern and mass transfer mechanism inside the device will be investigated.

With such a complex flow, in order to accomplish this aim, a progressive approach is required. The flow of *Power Law* fluids in pipes has been deeply studied and the analytical solutions are well known. Therefore, the first step is to study the effect of inserting a rod inside a pipe (concentric annulus geometry). The flow of a *Power Law* fluid in this geometry will be studied by means of a numerical model. In the second step, the effect of the semi-circle shaped scrapers in the non-Newtonian flow will be visualized by using Particle Image Velocimetry.

When the Pi theorem is applied to the mechanical problem (study of pressure drop), it is found to depend on the following non-dimensional numbers: the Reynolds number Re_b and the fluid behaviour index n, a rheological parameter of the *Power Law* model.

Table 1
Generalized Reynolds number constants values for the device under study (pipe with insert device).

a	b
262.27	−2.1177

In a previous paper [10], a Generalization method was defined for the device under study, in the case where the insert device is static. The method reduces the complexity of the problem, by including the dependence on n in the definition of the Generalized Reynolds number (Re_g). The suitability of this method for the case of a moving insert device, depends, among other conditions, on the flow structure. The Generalization method is to be applicable, only in cases where the flow structure does not vary significantly from the case with the static device. This point has also been studied in the current paper.

2. Experimental Setup

The purpose of the experimental facility shown in Fig. 2 is to obtain the velocity field of the pseudoplastic fluid which flows through a tube with an inserted device (Fig. 1). Its main section
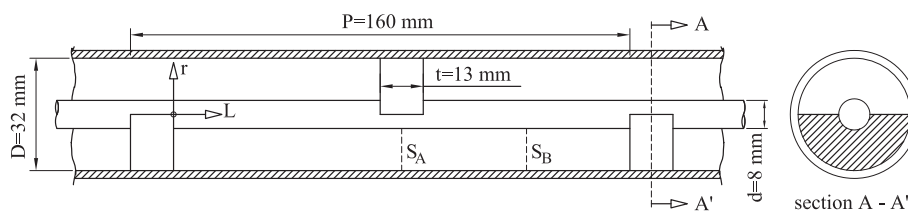
Fig. 1. Geometry of the device.
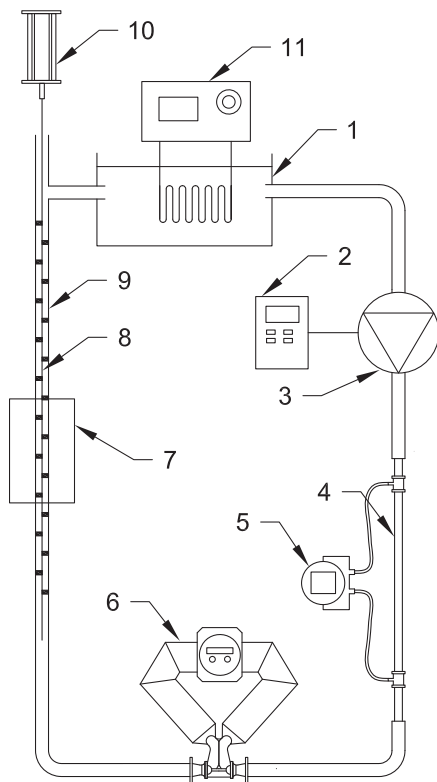
Fig. 2. Experimental apparatus. (1) Reservoir tank, (2) frequency converter, (3) gear pump, (4) in line viscometer, (5) differential pressure sensor, (6) Coriolis flowmeter, (7) visualization box, (8) insert device, (9) acrylic pipe, (10) hydraulic cylinder, (11) electric heater.

consists of a 32 mm diameter acrylic tube. The test section is located within a distance of 30 diameters from the tube inlet in order to ensure periodic flow conditions. To improve the optical access to this section, a flat-sided acrylic box has been placed, which has been filled with water. The test fluid is a water solution of a 1% concentration of CMC, which will be described in Section 2.1. A gear pump, regulated by a frequency converter, pumps the viscous fluid through the circuit loop. This allows the regulation of the flow rate, which will be measured by a Coriolis flowmeter. In order to control the fluid temperature, there is an electric heater in the upper reservoir tank.

In order to obtain the flow field, the Particle Image Velocimetry technique is employed [15]. To that end, the flow is seeded with 57 microns average diameter polyamide particles with a density of 1.016 kg/l. A laser illuminates the symmetry plane of the flow (see Fig. 3). The camera is situated in orthogonal position in relation to that plane, so that it can have a front view of it. Taking two consecutive images of the particles and knowing the time gap between them, the 2-dimensional velocity field can be obtained.

The 1 mm thick plane laser light is pulsed at 100–500 Hz in order to obtain multiple pairs of images. Its wavelength is 808 nm. The 1280×1024 pix^2 CMOS camera, together with a 20X optical zoom lens, provides images with a resolution of 0.191 mm/pix. The pictures are taken in pairs, triggered by the movement of the scraping device. For each experiment in dynamic conditions, 200 pairs of images have been processed. In static conditions a total of 200 consecutive images have been obtained, which leads to 199 pairs of images. The image sets have been processed using the software VidPIV, which uses the *Cross Correlation* and *Adaptive Cross Correlation* algorithms and a progressive

reduction of the interrogation areas. As a result, a flow field is obtained for every pair of images. The final result is obtained as an average of the individual results for each pair of images.

The laser light is 100 mm high but the technique can only give good results in a region 80 mm high, where the illumination quality is optimal. Therefore, the results are processed in three regions as shown in Fig. 3, with an overlap of 20 mm between them.

In dynamic experiments, the reciprocating motion of the insert device has constant and practically equal velocities in each direction and an amplitude of 200 mm ($8.3D_h$). The rod is moved by the hydraulic system depicted in Fig. 2. Further information on this aspect is given by Solano et al. [17] and Crespí-Llorens et al. [9]. The two directions of the movement of the insert device will be called, from now on, co-current and counter-current, which relates them to the direction of the flow.

The high speed camera is configured to take pairs of pictures in co-current or counter-current direction of the scraper. It is triggered by the combination of an optical sensor, placed in the lower end of the insert device, and a timer. This allows us to configure the trigger for regions A, B and C in both directions of the scraper. The images of the three regions are taken so that the scraper always appears in them, acting as reference point (see Fig. 3).

In the experiments the flow rate ranges from 280 l/h to 355 l/h and temperatures between 25 °C and 30 °C have been used. A further increase in the fluid temperature would have meant a quicker degradation due to the thermal treatment. Besides, different scraping velocities have been studied: $|v_s| \in [0; 0.261]$ m/s and $0 \leqslant |v_s/u_b| \leqslant 3$.

The uncertainty of the obtained velocity field has been measured at two axial positions, in static ($v_s = 0$) and dynamic ($v_s \neq 0$) conditions. On the one hand, the uncertainty of a measurement obtained from a pair of images is shown in Fig. 4(a). The maximum uncertainties do happen in the interrogation areas next to the pipe walls or the axis, being $s(u_i)/u_i = 83\%$ for the static experiments and $s(u_i)/u_i = 43\%$ for the dynamic ones. This high uncertainty near the walls is characteristic of PIV measurements, due to the high velocity gradients and light reflections. On the other hand, the maximum uncertainty associated, after averaging out the results of all the image pairs, is of $s(U_i)/U_i = 5\%$ for the static experiments and $s(U_i)/U_i = 4\%$ for the dynamic ones (see Fig. 4(b)).

The rheological properties of the non-Newtonian test fluid n and m are measured by an in-line viscometer. In that way, measurements of the rheological properties could be carried out at the beginning and at the end of each experiment, minimizing the thixotropy effect. The procedure to measure the rheological properties has been detailed previously by the authors [10]. The maximum uncertainty of the measurements of n and m are 0.01% and 0.4% respectively. The uncertainty of Re_b is 1%, while the uncertainty of Re_g is given by the uncertainty of the experimental Generalization method, being 11% [10].

2.1. Test fluid characteristics

The test fluid was 1 %wt aqueous solutions of carboxymethyl cellulose (CMC), supplied by SigmaAldrich Co. CMC with different chain length have been used: medium viscosity (Ref. C4888, 250 kDa), high viscosity (Ref. C5013, 700 kDa) and ultra high viscosity (Ref. 21904). The solutions were prepared by dissolving the polymer powder in distilled water and then raising the pH values of the solution to increase viscosity. This fluid shows a non-Newtonian pseudoplastic behaviour well described by the *Power Law* model of Eq. (1) for a wide range of shear rates [1,12,2,22].
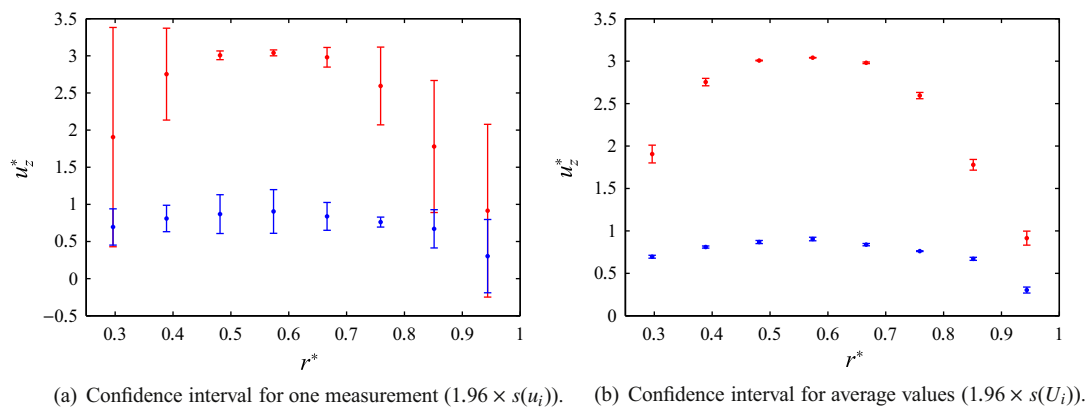
$$\tau = m\gamma^n \tag{1}$$
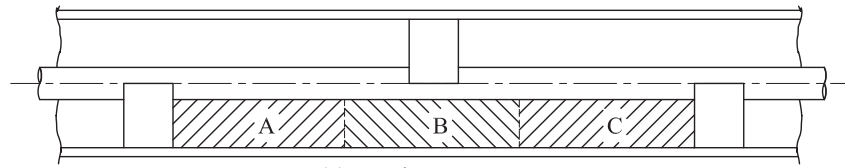
(a) Regions arrangement.
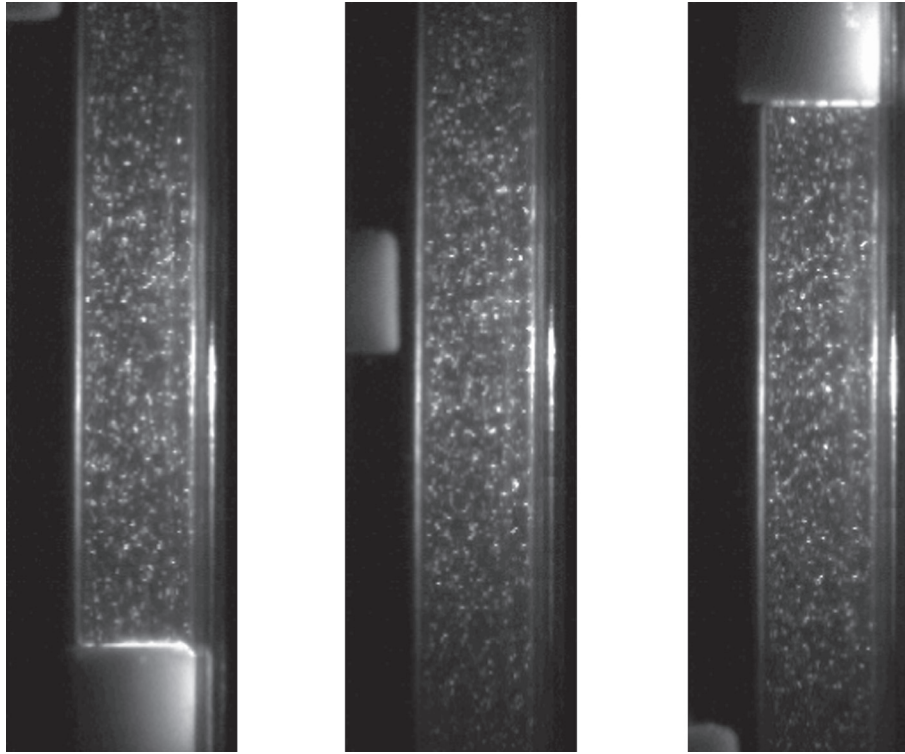
(b) PIV samples of the captures in regions A, B and C (from the left to the right).

Fig. 3. Regions of the PIV captures.

(a) Confidence interval for one measurement ($1.96 \times s(u_i)$).

(b) Confidence interval for average values ($1.96 \times s(U_i)$).

Fig. 4. Confidence interval for a confidence level of 95%. Velocity profiles at axial positions $z = 4P/5 - t_s$ and $z = (P - t_s)/2$, in red and blue respectively. Experiments in static conditions ($n = 0.52$ and $Re_b = 1.4$). (For interpretation of the references to colour in this figure legend, the reader is referred to the web version of this article.)

All CMC thermophysical properties except for the rheological parameters and fluid density were assumed to be the same as pure water [8,7].

Rheological fluid properties are strongly influenced by the type of CMC powder employed, the preparation method and fluid degradation due to shear stress and thermal treatment. The combination of those factors allows us to obtain fluids with different pseudoplastic behaviour, $3.5 \text{ Pa s}^n \geqslant m \geqslant 0.07 \text{ Pa s}^n$ and $0.52 \leqslant n \leqslant 0.94$.

3. Numerical model

The numerical model provides the fully developed velocity profile and pressure drop of the axially circulating flow through

concentric annulus. The rheology of the fluid follows the *Power Law* model, being the flow laminar, incompressible, stationary and isothermal.

As explained by Chhabra and Richardson [8] the resolution of the velocity profile for this flow, in the fully developed region, leads to an integral expression which cannot be solved for every value of *n*. Hanks and Larsen [13] solved the integrals numerically for some values of *n* and the ratio of diameters α and the inner rod in static conditions. However, for this investigation, the solutions for a moving rod, $\alpha = 0.25$ and the flow behaviour index of the fluids used in the experiments (*n*) are required. This model has been implemented to avoid this inconvenience, allowing us to obtain the velocity profile of the fully developed flow for different flow properties and rod velocities. Besides, it also provides its pressure drop per linear meter.
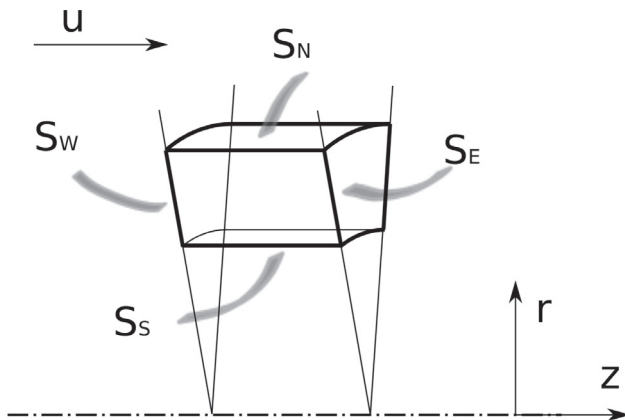
By considering stationary conditions and that, in the fully developed region, the flow is axisymmetric, the continuity equation simplifies to

$$\frac{\partial u_z}{\partial z} = 0 \qquad (2)$$

By applying the former considerations, the continuity equation itself and the *Power Law* model definition of the shear stress, the momentum equation in the axial direction becomes
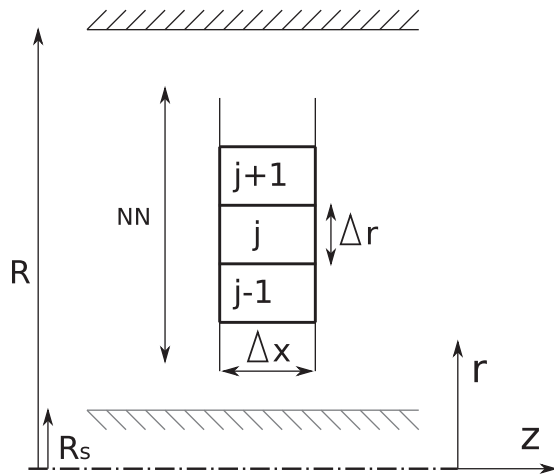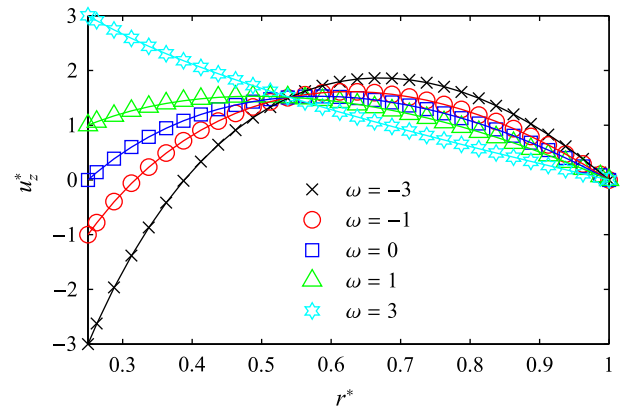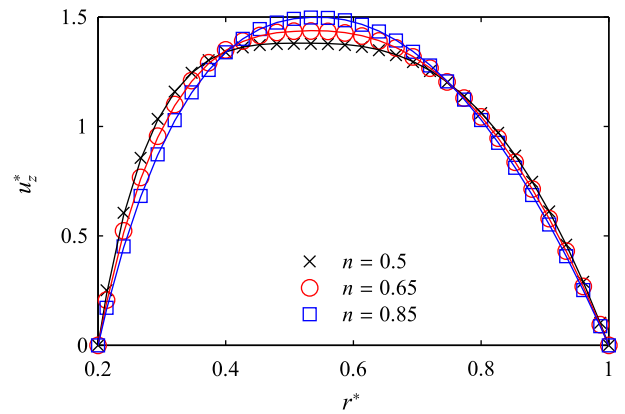
(a) Mesh.

(b) Finite volume surfaces.

Fig. 5. Fluid space discretization.

(a) Newtonian fluid and different velocities of the axis.

(b) Non-Newtonian fluid.

Fig. 6. Validation of velocity profiles in concentric annulus geometry. The inner axis can move at a non-dimensional velocity of $\omega = v_s/u_b$. Legend: numerical model results are represented with symbols and the reference solution with lines.

Table 2
Deviations between the results of the numerical model and the reference solution. Velocity Deviations defined as a percentage of u_b.

NN	ω				
	−3	−1	0	1	3
(a) Velocity profile for the Newtonian flow (n = 1). $\alpha = 0.25$					
30	1.11%	0.67%	0.46%	0.24%	0.19%
50	0.42%	0.26%	0.17%	0.09%	0.07%
100	0.11%	0.07%	0.05%	0.02%	0.02%
200	0.03%	0.02%	0.01%	<0.01%	<0.01%

NN	*n*		
	0.5	0.65	0.85
(b) Velocity profile for $0.5 \leqslant n < 1$. $\alpha = 0.2$			
30	1.85%	1.24%	0.78%
50	0.73%	0.49%	0.30%
100	0.19%	0.30%	0.10%
200	0.05%	0.32%	0.12%

NN	*n*			
	0.5	0.65	0.85	1
(c) Pressure drop, f_∞. $\alpha = 0.25$				
30	1.30%	1.01%	0.59%	0.26%
50	1.13%	0.84%	0.42%	0.09%
100	1.05%	0.77%	0.35%	0.02%
200	1.03%	0.75%	0.33%	<0.01%

$$\frac{\partial p}{\partial z} = \frac{1}{r}\frac{\partial (r\tau_{rz})}{\partial r} = \frac{1}{r}\frac{\partial}{\partial r}\left(rm\left(\frac{\partial u_z}{\partial r}\right)^n\right) \tag{3}$$

The previous equations describe the developed flow of a *Power Law* fluid flowing through a concentric annulus, where the inner rod can move in axial direction. Because of the non-slip condition at the walls,

$$r = d/2 \rightarrow u_z = v_s \tag{4}$$
$$r = D/2 \rightarrow u_z = 0 \tag{5}$$

In order to apply a CFD method, a mesh has been defined. It consists of a slice of the pipe, which has been divided axially in NN finite volumes, like the one in Fig. 5(b). The points $j = 1$ and $j = NN + 2$ are the contact points between the rod and the flow and between the pipe and the flow respectively. The centre points of the finite volumes, indexed from $j = 2$ to $j = NN + 1$, are in between. Using the finite volumes method the momentum equation is discretized, leading to the following equation system

$$u_1 = v_s \tag{6}$$

$$\mu_S u_{j-1}\frac{S_S}{\Delta r_S} - \left(\mu_S \frac{S_S}{\Delta r_S} + \mu_N \frac{S_N}{\Delta r_N}\right)u_j +$$
$$+ \mu_N u_{j+1}\frac{S_N}{\Delta r_N} + p_L V = 0 \tag{7}$$

$$u_{NN+2} = 0 \tag{8}$$
$$\sum u_j S_E = Q \tag{9}$$

being, for every finite volume, the viscosity of the south and north faces as follows

$$\mu_S = m\left(\frac{u_j - u_{j-1}}{\Delta r_S}\right)^{n-1}; \quad \mu_N = m\left(\frac{u_{j+1} - u_j}{\Delta r_N}\right)^{n-1} \tag{10}$$

where Eqs. (6) and (8) are the boundary conditions at the walls (points $j = 1$ and $j = NN + 2$ respectively). Eq. (7) is the momentum equation which will be applied for $j = [2, NN + 1]$. Finally, Eq. (6) is the continuity equation: the sum of the flow rates through the different volumes should be equal to the total flow rate (Q).

The algorithm to solve the equation system works as follows. In the first iteration, it considers the fluid to be Newtonian, $n = 1$ and $\mu_N = \mu_S = m$, and solves the equation system, thus obtaining the velocity profile for a Newtonian fluid. If the fluid is non-Newtonian, an iterative process starts:

1. Obtain the viscosity profile (μ_S and μ_N) using the velocity profile from previous iteration.
2. Solve the equation system considering the non-Newtonian behaviour ($n \neq 1$).
3. Obtain pressure drop out of the velocity gradient at the wall.
4. Check convergence by comparing pressure drop of the current and previous iterations.

3.1. Validation of the model

To validate the model, the available solutions for the annulus geometry are used. The process has been carried out in three steps:

1. Validation of the velocity profile for a Newtonian fluid, where the analytical solution can be obtained for different velocities of the axis.
2. Validation of the velocity profile for a non-Newtonian fluid. The results are compared with the ones obtained numerically by Hanks and Larsen [13].
3. Validation of pressure drop. Results are compared to the approximated expression obtained by Kozicki et al. [14].

Validation results are shown in Fig. 6 and the corresponding deviations between the reference solution and the model in Table 2. They show a good performance of the model when $NN = 100$: deviations in the velocity profile are below 0.3% and deviations in pressure drop are below 1%. Considering that the expression from Kozicki is an approach and not an exact solution for $n \neq 1$, it can be concluded that the model is valid and precise.

4. Results

In a previous investigation with Newtonian fluids [17] determined that the *blockage factor* β, is the most significant non-dimensional parameter for the velocity of the scraper v_s. It is defined as follows, and expresses whether the scraper, with its movement, is blocking or helping the fluid flow.

$$\beta = \frac{u_b - v_s}{u_b} = 1 - \frac{v_s}{u_b} \tag{11}$$

Thus,

- If $v_s = u_b$ then $\beta = 0$ and the scraper is not blocking nor helping the flow. This case can occur only in the co-current movement of the scraper.
- If $v_s < u_b$ then $\beta > 0$ and the scraper is blocking the flow. This case occurs when the scraper:
  - ...moves in counter-current direction ($v_s < 0$).
  - ...is static ($v_s = 0$).
  - ...moves in co-current direction and $v_s < u_b$.
- If $v_s > u_b$ then $\beta < 0$ and the scraper is helping the fluid flow. This case can occur only in the co-current movement of the scraper.

The non-Newtonian behaviour of the test fluid does not change these three structures of the flow field. The structures are shown in Fig. 7, where, for each case, an example of the flow field is presented.
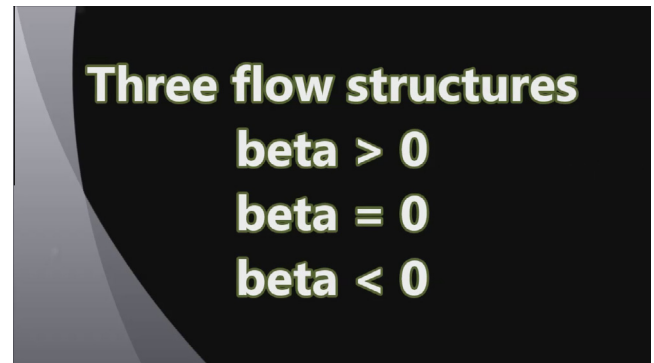
Video 1. The three possible structures of the flow: $\beta > 0$, $\beta = 0$ and $\beta < 0$.

For the case of $\beta < 0$, the scraper moves in co-current direction and quicker than the flow (u_b). Consequently, an overpressure is generated downstream of the scraper and an under-pressure upstream of it. If compared to the pressure drop in concentric annulus, this should result in a lower or even negative pressure drop. In Fig. 7(c), zones $Z1$ (downstream of the scraper), $Z2$ (opposite the scraper) and $Z3$ (upstream of the scraper) have been highlighted. On the one hand, the flow pattern shows a co-current flow which connects zone $Z1$ and zone $Z3$ of consecutive scrapers in opposite positions. On the other hand, in zone $Z2$ a counter flow can be observed. This flow structure shows a significant mass transfer between core and peripheral regions.
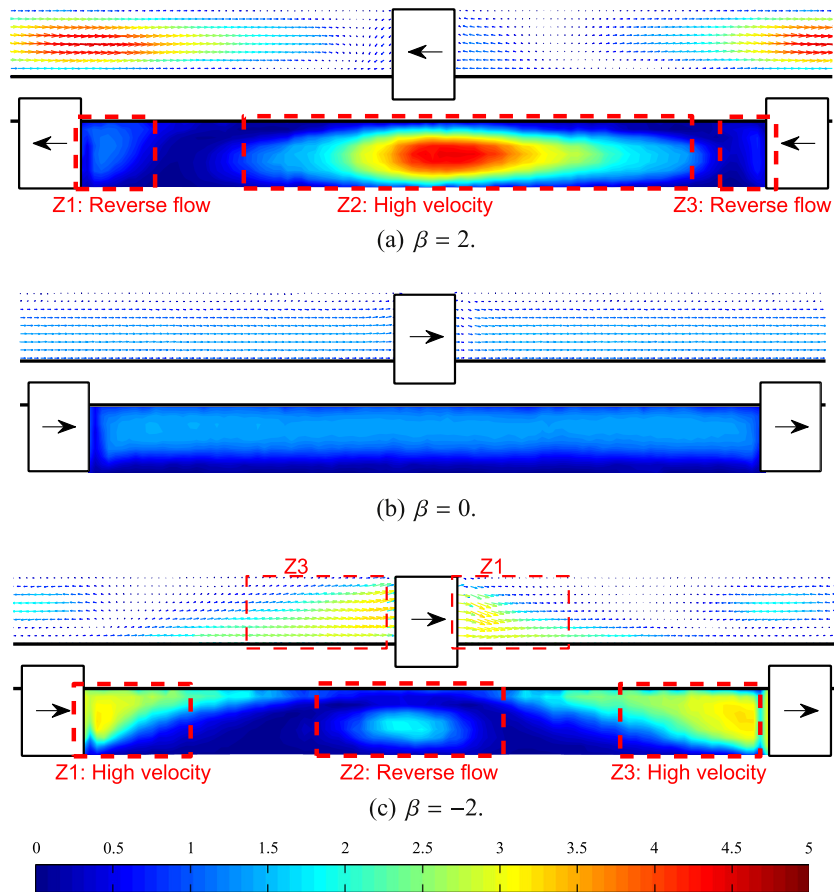
(a) $\beta = 2$.

(b) $\beta = 0$.

(c) $\beta = -2$.

Fig. 7. Effect of the *blockage factor* on the flow pattern. Non dimensional flow pattern ($\bar{v}/u_b$) for experiments with $Re_b \approx 4.5, n \approx 0.63$. Experiments D-3, S-2 and D-7.

If the scraper moves in co-current direction with the average velocity of the flow, $\beta = 0$, the flow pattern is very similar to the one in the concentric annulus geometry. In this case, pressure drop should also be similar, as the scrapers are not generating additional pressure variations. Furthermore, no relevant mass transfer is observed between the inner and outer regions of the flow.
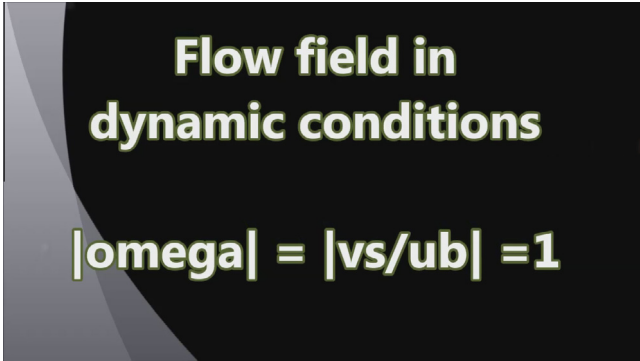
The third case is when $\beta > 0$ and the fluid flow is being blocked by the scraper, which is slower than the fluid, static or otherwise, it moves in counter-current direction. In any of these situations the flow pattern is quite similar, its main characteristic being the high velocities in zone Z2. Besides, low or counter-current velocities can be observed in regions Z1 and Z3 close to the scraper, due to the low pressure in region Z1 (downstream of the scraper) and the high pressure in region Z2. If compared to the pressure drop in concentric annulus, the pressure differences generated by the scrapers will result in higher pressure drop in the pipe with the insert device [10]. Besides, a remarkable mass transfer between core and peripheral regions is observed.

In the following subsections, these three different patterns will be analysed in detail. The influence of the Reynolds number and the fluid behaviour index n will be evaluated, as well as the impact of the variation of the blockage of the flow β in the three different cases. Special attention will be paid to the case of the static scraper ($v_s = 0$ and $\beta = 1$), where no external power is required.

In dynamic conditions of the scraper ($\beta \neq 1$), the different sign of the velocity of the scraper v_s in co-current and counter-current movements implies different values of β. This can lead to different flow structures in each half of the cycle.

Table 3
Experiments in static conditions of the scraper ($\beta = 1$).

Id. no.	Q (l/h)	n	m (Pa s^n)	Re_b	Re_g
S-1	280	0.52	3.50	1.4	5
S-2	318	0.621	0.987	5.2	15
S-3	347	0.682	0.576	9	23
S-4	355	0.944	0.0695	49	60

Video 2. Full working cycle for $|v_s| = u_b$, resulting in $\beta = 0$ and $\beta = 2$ in co-current and counter-current directions respectively.
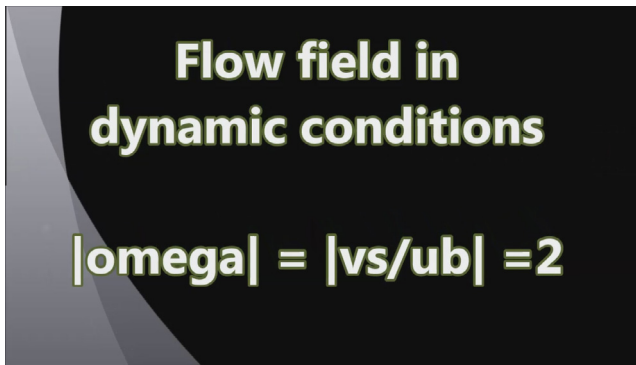
Video 3. Full working cycle for $|v_s| = 2 \times u_b$, resulting in $\beta = -1$ and $\beta = 3$ in co-current and counter-current directions respectively.

In order to study the influence of the variables of the problem in the flow pattern, the experiments will be carried out in the following ranges of the significant non-dimensional variables:

- $Re_b \in [1.4, 49]$.
- $n \in [0.52, 0.94]$.
- $\beta \in [-2, 4]$.

Specific details of the experiments in static and dynamic conditions of the scraper are given in Tables 3 and 4 respectively.

The main practical problem which has been faced is the difficulty to control the rheological properties of the fluid, which depend on: the chain length of the CMC employed, the preparation method, the temperature of the fluid and its degradation. The longer the fluid is used, the higher the degradation, which is specially sensible to thermal treatment. This has made impossible in practice to study the variation of the Reynolds number and n independently. This highlights the importance of a proper definition of the Generalized Reynolds number for the study of pressure drop and heat transfer, which reduces greatly the complexity of the problem.

4.1. Flow description for $\beta = 0$

As mentioned before, in this case, the scraper moves in the direction of the flow and with its bulk velocity ($v_s = u_b$). The flow pattern has been found to be very similar to the one in a concentric annulus geometry (see Fig. 7(b)). In order to confirm this, the velocity profiles are presented in Fig. 8 for experiments with different Re_b and n, and compared to the velocity profiles in annulus geometry. As shown in the figure, the velocity profiles change with n, increasing its maximum velocity when n increases. As the changes of the velocity profiles can be explained by the change in n, the influence of the Reynolds number is considered to be non-existent in this range (laminar flow). As velocity profiles are similar to the ones in a concentric annulus geometry, the pressure drop and its dependence on n are also expected to be similar.

In the followings sections, for $\beta \neq 0$, it will be shown that the Reynolds number has greater impact on the flow field, while the influence of n is similar to this case.

### 4.2. Flow description for $\beta > 0$

As stated before, three different cases of $\beta > 0$ will be considered. For all three cases, the flow structure is similar. The limiting case is the one described in the previous section ($\beta = 0$), which occurs in co-current movement of the scraper when $v_s = u_b$. If the scraper moves in co-current direction and $v_s < u_b$, then the blockage factor will be $0 < \beta < 1$. The second case is when the scraper does not move, where $\beta = 1$. The last case occurs when the scraper moves in counter-current direction and $\beta > 1$. For these three cases, the flow changes progressively, from the case of $\beta = 0$ where the influence of the scraper on the flow is practically non-existent to the case of $\beta > 1$ where the scraper effect on the flow pattern is significant. The more significant, the greater the value of β. This effect can be observed in Fig. 9 and more in detail in following sections. The figure also shows how the mass transfer between core and peripheral regions increases with β. Similarly, pressure drop will increase progressively with β, as the pressure difference created by the scrapers increase; Solano et al. [17]

Table 4
Experiments in dynamic conditions of the scraper. Re_g: note that the applicability of the generalization method to experiments in dynamic conditions of the scraper is studied in this paper.

Id. no.	$\omega = v_s/u_b$	$\beta = 1 - \omega$	Q (l/h)	u_b (m/s)	v_s (m/s)	n	m (Pa s^n)	Re_b	Re_g
D-1	0.5	0.5	210	0.077	0.039	0.61	0.767	3.8	12
D-2	1	0	210	0.077	0.077	0.61	0.736	4.0	12
D-3	2	−1	210	0.077	0.155	0.62	0.706	4.1	12
D-4	3	−2	210	0.077	0.232	0.63	0.675	4.3	12
D-5	−0.5	1.5	210	0.077	−0.039	0.62	0.689	4.2	12
D-6	−1	2	210	0.077	−0.077	0.64	0.643	4.4	13
D-7	−2	3	210	0.077	−0.155	0.65	0.597	4.7	13
D-8	−3	4	210	0.077	−0.232	0.66	0.551	5.1	14
D-9	−0.5	1.5	226	0.083	−0.042	0.76	0.231	12	25
D-10	−1	2	226	0.083	−0.083	0.77	0.215	12	25
D-11	−2	3	226	0.083	−0.167	0.78	0.199	13	26
D-12	−3	4	226	0.083	−0.250	0.79	0.183	14	28
D-13	0.5	0.5	226	0.083	0.416	0.79	0.183	14	28
D-14	1	0	226	0.083	0.083	0.79	0.181	14	28
D-15	2	−1	226	0.083	0.167	0.79	0.178	15	28
D-16	3	−2	226	0.083	0.250	0.795	0.176	15	28
D-17	0.5	0.5	236	0.087	0.044	0.85	0.0805	32	51
D-18	1	0	236	0.087	0.087	0.86	0.0800	31	49
D-19	2	−1	236	0.087	0.174	0.87	0.0794	31	48
D-20	3	−2	236	0.087	0.261	0.87	0.0789	31	48
D-21	−0.5	1.5	236	0.087	−0.044	0.87	0.089	28	43
D-22	−1	2	236	0.087	−0.087	0.88	0.0821	30	44
D-23	−2	3	236	0.087	−0.174	0.88	0.0815	30	44
D-24	−3	4	236	0.087	−0.261	0.89	0.0810	30	43
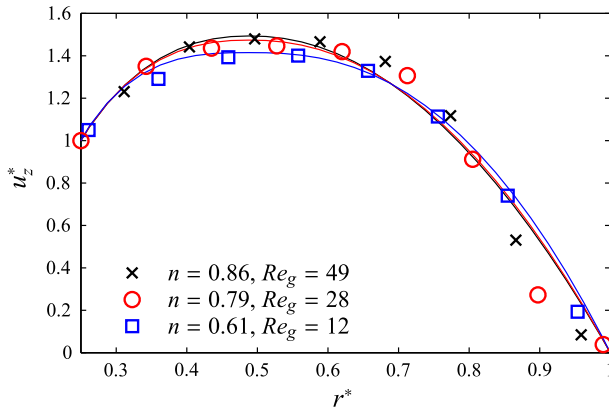
Fig. 8. Velocity profiles comparison for $\beta = 0$ in section S_A at $z = 3(P - t_s)/4$ downstream of the scraper. Experiments D-18, D-14 and D-2. Symbols: pipe with scraping device (experimental results). Lines: concentric annulus geometry (numerical results).

detected this pressure drop increase working with Newtonian fluids and the authors, working with non-Newtonian fluids, measured high pressure drops for $beta = 1$ [10], which are also dependent on n.

In the case where the apparatus is working with low scraping velocities $|v_s| < u_b$, the *blockage parameter* β is positive for co-current and counter-current semi-cycles of the scraper ($0 > \beta > 2$). This leads to similar flow structures for the full working cycle. Therefore, the Generalization method defined by the authors [10] for the static conditions of the scraper ($\beta = 1$) is potentially suitable for this working regime ($|v_s| < u_b$ and $0 < \beta < 2$).

4.2.1. Case of static scraper ($\beta = 1$)

The use of the insert device inside the pipe has two main purposes: to avoid fouling formation and to enhance heat transfer. Its main drawback is the power consumption required to move the insert device [18]. Therefore, in many cases, it may be interesting for the device to scrape only sporadically, minimizing power consumption while avoiding fouling formation. If this is the case, the insert device will be static most of the time, and thus the importance of this section.

Flow fields of three experiments with increasing Re_b and n values are shown in Fig. 10. The structure of the flow for experiments with positive blockage factor has been described earlier in Section 4 (see Fig. 7(a)). This structure shows a high velocity region where the cross section is reduced to the half by the presence of the scraper (zone Z2). As it can be observed, when increasing Re_b and

(a) Case $\beta = 0$.

(b) Case $\beta = 0.5$.

(c) Case $\beta = 1$ (static).

(d) Case $\beta = 2$.
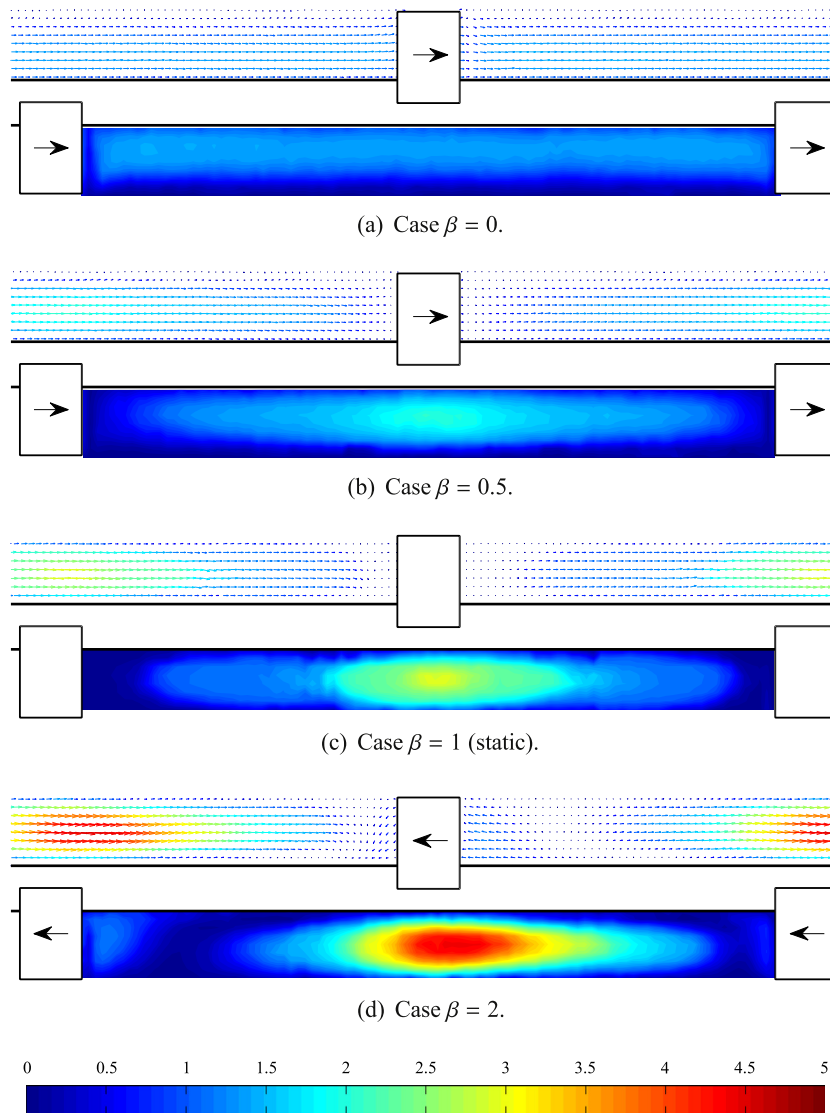
Fig. 9. Flow pattern for $\beta > 0$. Experiments D-2, D-1, S-2 and D-3 with $Re_b \approx 4.5$, $n \approx 0.63$.

(a) $Re_b = 1.4$, $Re_g = 5$, $n = 0.52$.

(b) $Re_b = 9$, $Re_g = 23$, $n = 0.68$
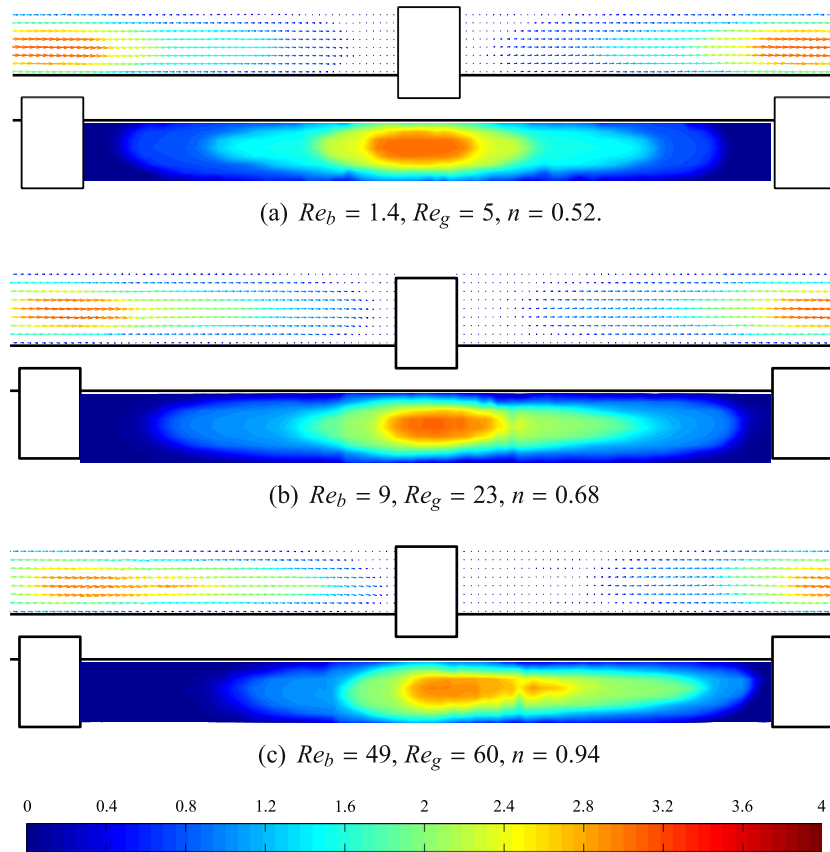

(c) $Re_b = 49$, $Re_g = 60$, $n = 0.94$

Fig. 10. Flow pattern in static conditions of the scraper ($\beta = 1$). Experiments S-1, S-3 and S-4.

n, the high velocity region moves downwards. This same behaviour has been detected by Solano et al. [17], who related it to the increase of the Reynolds number.

In order to evaluate the influence of n, a comparison with the results in the concentric annulus geometry has been made in Fig. 11. For both cases, the velocity profile is plotted in sections S_A and S_B, located at distances of $z = (P - t)/2$ and $z = 3(P - t)/4$ downstream of the scraper (see location of the sections in Fig. 1). The velocity profiles shown in Fig. 11 show that, for the annulus geometry, the velocity profiles of the fully developed flow depend on n, being sharper the greater the value of n is. However, this behaviour cannot be detected in the pipe with the insert device, where the effect of the Reynolds number is far more significant, specially in section S_B. The maximum velocity in section S_A is around three times greater than the bulk velocity. In this section the velocity profiles are sharper when increasing n and Re_b, but no final conclusion can be reached. In section S_B, the maximum velocity increases significantly with Re_b, due to the downstream displacement of the high velocity region (Z2). For the experiment with the lower Reynolds number, the velocity profile is almost identical to the one in an annulus geometry ($u_z^* = 1.4$), while for the experiment with the higher Reynolds number, the maximum velocity increases up to $u_z^* = 2.2$. By the comparison with the results in the annulus geometry the conclusion is that this increase in the maximum velocity is caused by the increase in the Reynolds number, Re_b.

According to the flow patterns shown in Fig. 10, the low velocity zones (Z1 and Z3) vary in size with the Reynolds number (and n). A study of this variation is shown in Fig. 12. The contour represented in the figure corresponds to a non-dimensional velocity of $u_z^* = 0.25$. The election of this limiting value is not relevant, as the velocity gradient in this area is high. As it can be observed, the size

of zone Z1 (downstream of the scraper) increases with the Reynolds number, while the opposite happens to the size of zone Z3 (upstream of the scraper). This increase and decrease of both zones with Re_b is non-linear (see Fig. 12(g)), which is logical due to the limited distance between consecutive scrapers on the same side of the pipe.

4.2.2. Case of the scraper in co-current direction $0 < \beta < 1$

In this situation, for $\beta = 0.5$, the results show a flow pattern (Fig. 9(b)) in between the two limiting cases. For the limiting case of $\beta = 0$, the influence of the scraper is minimum. When β increases, so does the influence of the scraper in the flow until the case of $\beta = 1$ which has been studied in previous section.
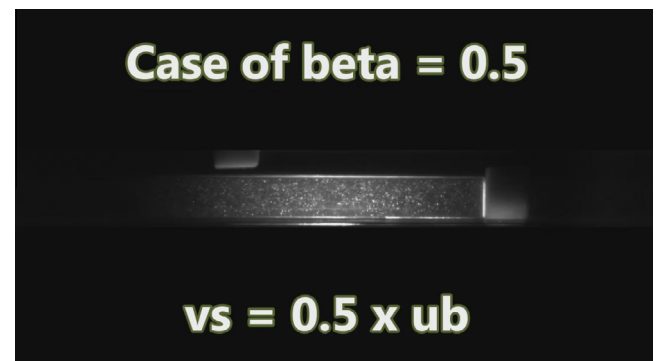
Video 4. Case of $\beta > 0$ in co-current direction ($0 < \beta < 1$). The case of $\beta = 0.5$ is compared to the limiting cases ($\beta = 0$ and $\beta = 1$).

(a) Section S_A, at $z = (P - t)/2$.

(b) Section S_B, at $z = 3(P - t)/4$.
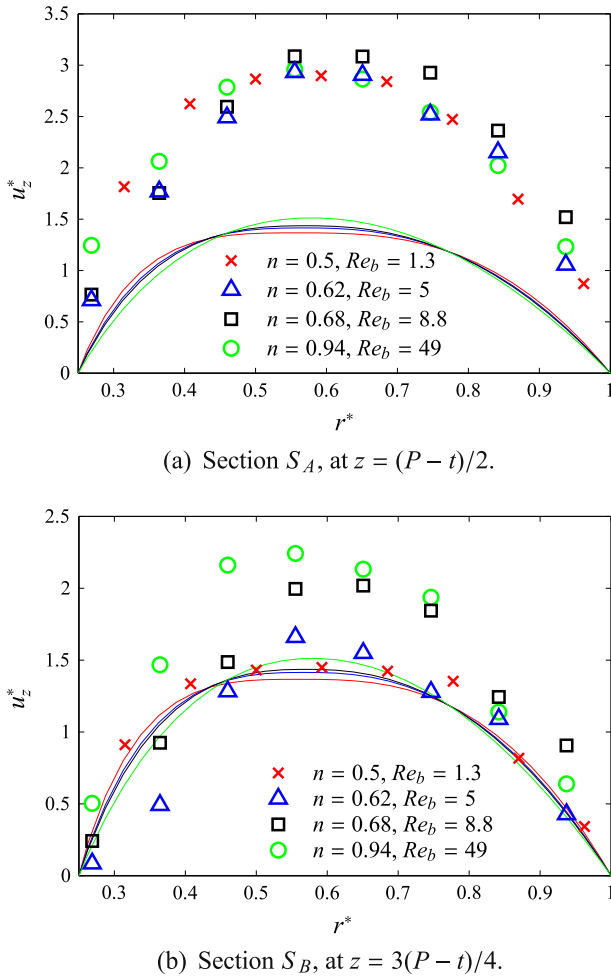
Fig. 11. Velocity profiles comparison for $\beta = 1$ (static device). Experiments S-1 to S-4. Symbols: pipe with scraping device (experimental results). Lines: concentric annulus geometry (numerical results).

Three experiments for $\beta = 0.5, n \in [0.61 - 0.86]$ and $Re_b \in [3.9, 14]$ have been carried out and no significant difference has been detected on the flow pattern. For the three of them, the maximum velocity in the flow field (Fig. 9(b)) is around $2.2 \times u_b$. Besides, if the flow field is compared to the one in static conditions of the scraper (Fig. 9(c)), the following is detected:

- The low velocity areas, upstream and downstream of the scraper, are smaller in the present case.
- Velocity in this areas has increased due to the movement of the scraper.

Fig. 13 shows the velocity profiles in sections S_A and S_B for experiments with $\beta = 0, 0.5, 1$. The velocity profiles in section S_B are remarkably similar to the results obtained numerically for the annulus geometry. Furthermore, the maximum velocities for the three cases under comparison are around 1.4 times the bulk velocity. However, significant differences can be observed in section S_A, being the case of $\beta = 0.5$ in the middle point between the limiting cases:

- For $\beta = 0$, the maximum velocity is $1.4 \times u_b$ and the velocity profile is the same as in annulus geometry. As stated before, there is little or no effect of the scraper.
- For $\beta = 0.5$, the maximum velocity is $2.1 \times u_b$.
- For $\beta = 1$, the maximum velocity is $2.9 \times u_b$.

4.2.3. Case of the scraper in counter-current direction $\beta > 1$

In the counter-current movement of the scraper, the blockage is always positive and greater than one. Therefore, the flow structures are similar to the case of the static scraper ($\beta = 1$). The effect of the scraper on the flow pattern is stronger, the greater β is.

Experiments for $\beta = 1.5, 2, 3, 4$ have been carried out with $Re_b \in [4.3; 30]$ and $n \in [0.62; 0.89]$. In order to study the effect of β, Fig. 14 shows the velocity pattern and velocity profiles for experiments of similar Reynolds number and flow behaviour index. In the results, the following can be observed:

- For higher values of β, the high velocity region Z2 grows in size.
- The maximum flow velocity rises with β: for $\beta = 1.5$, $u^*_{z,max} = 3.3$, while for $\beta = 4$, the maximum velocity is greater than six times the bulk velocity, $u_{z,max} = 6.3$.
- The variation of the velocity profiles for the concentric annulus geometry, due to the movement of the inner rod, is much lower. Hence, the influence on the flow of the scraping pieces is quite significant.
- The counter-current movement of the scraper induces an under-pressure area downstream of the scraper (Z1), which leads to a reverse flow in this area.
- This reverse flow area grows in size and velocity with β.
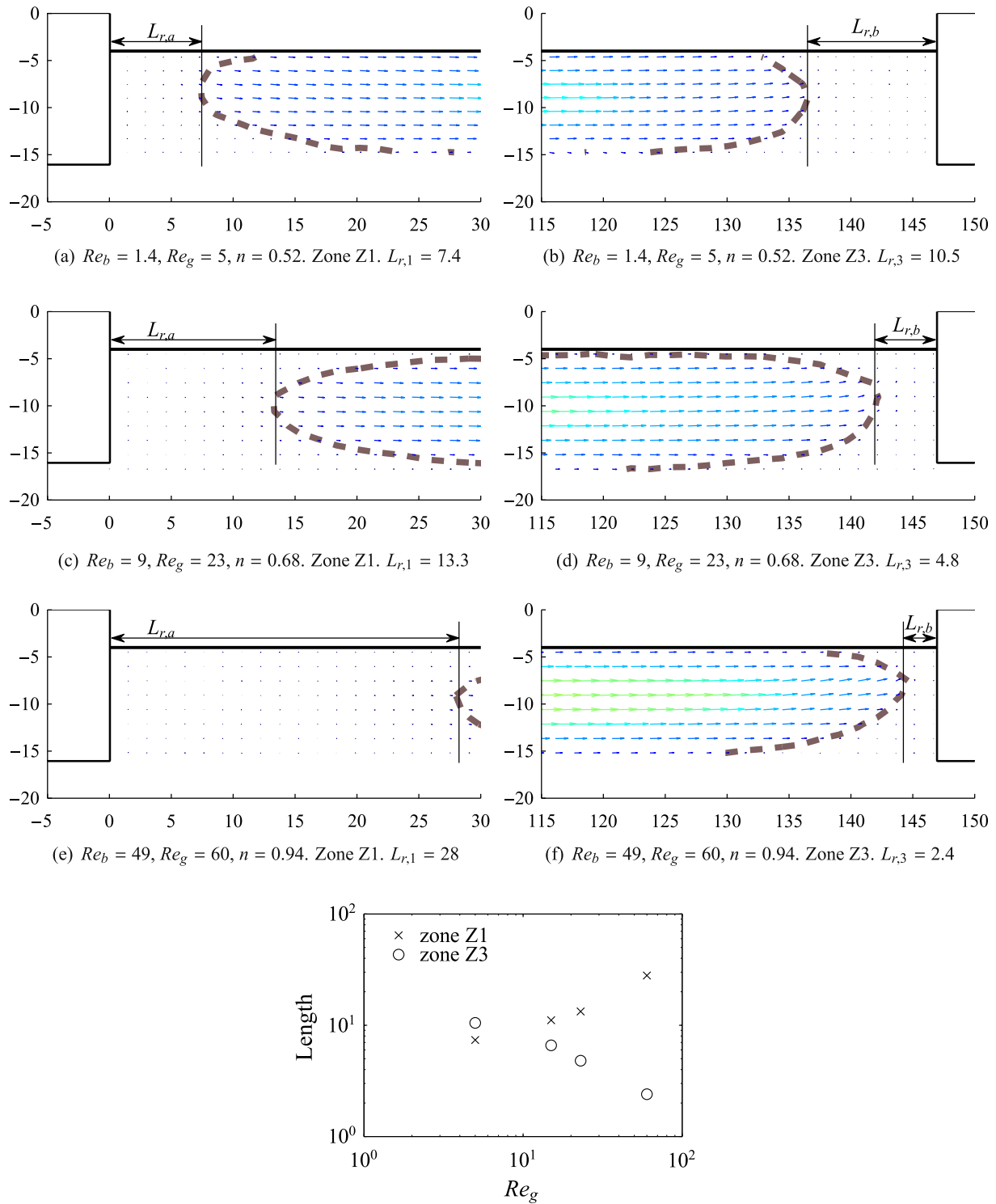- The importance of this behaviour in the area upstream of the scraper is small.

In order to study the influence of the Reynolds number and n, different experiments have been carried out for a constant value of $\beta = 4$, while varying the other two parameters. As in previous sections, together with the experimental results, the numerical results for the annulus geometry, working with the equivalent movement of the rod and the same pseudoplastic behaviour of the fluid, are presented in Fig. 15. The results show that when both the Reynolds number and n rise:

- The high velocity region of co-current flow (Z2) increases its size.
- The velocity profile at section S_A does not change significantly. These small changes do not correspond to the variation observed in the concentric annuli, which can also be explained by the Reynolds number increase.
- The velocity profile at section S_B shows that for the experiments with $Re_b = 5.1$, the velocity is lower. The reason is that the high velocity area is not long enough and does not influence this cross section. For the other two experiments, with higher Reynolds number, the velocity profile is similar and the maximum velocity is six times the bulk velocity. This effect is mainly due to the Reynolds number increase although the influence of n is always present.
- Zone Z1, downstream of the scraper, increases its size.
- The module of the velocities in zone Z1 (counter-current flow) are of the same order as the module of the velocities in zone Z2 (co-current flow).

As in previously analysed cases, all three non-dimensional variables, β, Re_b and n influence the flow pattern in the device under study. However, by comparison with the flow pattern in a concentric annulus, it has been found than the influence of β and Re_b is more important than the influence of n in the studied ranges.

4.3. Flow description for $\beta < 0$

This last case can only occur if the scraper moves in co-current direction of the flow, with $v_s > u_b$. As described before (Fig. 7(c)),

(a) $Re_b = 1.4$, $Re_g = 5$, $n = 0.52$. Zone Z1. $L_{r,1} = 7.4$

(b) $Re_b = 1.4$, $Re_g = 5$, $n = 0.52$. Zone Z3. $L_{r,3} = 10.5$

(c) $Re_b = 9$, $Re_g = 23$, $n = 0.68$. Zone Z1. $L_{r,1} = 13.3$

(d) $Re_b = 9$, $Re_g = 23$, $n = 0.68$. Zone Z3. $L_{r,3} = 4.8$

(e) $Re_b = 49$, $Re_g = 60$, $n = 0.94$. Zone Z1. $L_{r,1} = 28$

(f) $Re_b = 49$, $Re_g = 60$, $n = 0.94$. Zone Z3. $L_{r,3} = 2.4$

(g) Size of low velocity zones as a function of the generalized Reynolds number. Experiments S-1 to S-4.

Fig. 12. Reynolds number effect on the size of the low velocity zones.

the flow pattern changes drastically in this situation. On the one hand, the under-pressure (Z3) and over-pressure (Z1) regions created by the scraper movement, generate a co-current flow which links both regions. On the other hand, a counter flow may appear (depending on the value of β) in the region opposite the scraper.

As in previous sections, the effect of β will be analysed first. Fig. 16(c) corresponds to the limiting case of $\beta = 0$, where the insert device moves in co-current direction at $v_s = u_b$. In this case the device does not influence the flow pattern and no flow mixing takes place. Then, the lower β is, the greater the influence of the
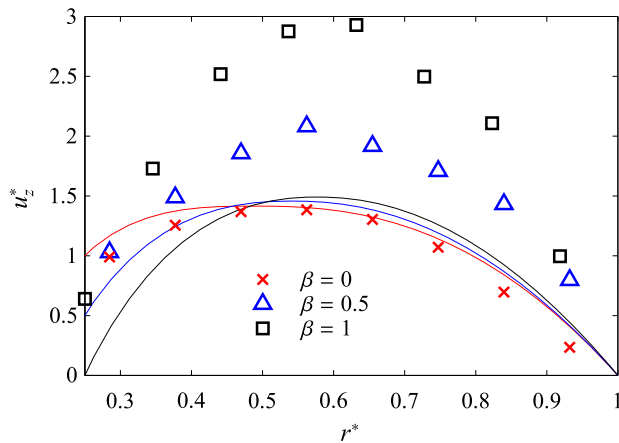
(a) Section S_A at $z = (P - t)/2$.
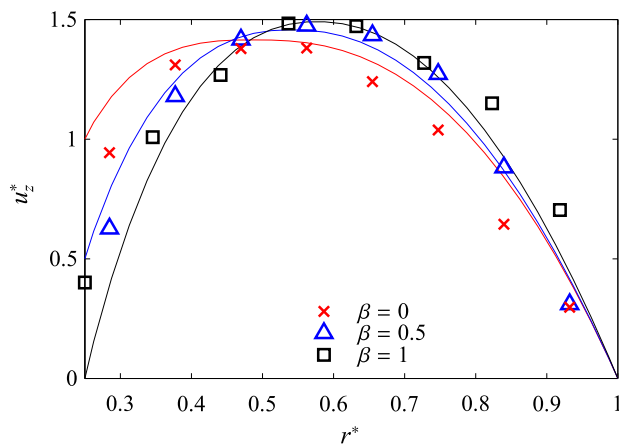
(b) Section S_B at $z = 3(P - t)/4$.

Fig. 13. Velocity profiles comparison between the case of $\beta = 0.5$ and the limiting cases of $\beta = 0; 1$. $Re_b \approx 4.2, n = 0.61 - 0.62$. Experiments D-2, D-1 and S-2. Symbols: pipe with scraping device (experimental results). Lines: concentric annulus geometry (numerical results).

scraper on the flow, which results in an increase of mass transfer between its core and peripheral regions. In both experiments, at $\beta = -1$ and $\beta = -2$, the maximum measured velocities are similar to the velocity of the insert device. The latter can be perceived in Fig. 16(d), where the scraper moves at $v_s = 2 \times u_b$ and in Fig. 16 (e), where it moves at $v_s = 3 \times u_b$. In the region opposite the scraper, a reverse flow appears for both experiments. This can be observed in Fig. 16(a) (section S_A), where small negative velocities in z direction are plotted for the case of $\beta = -1$, while in the case of $\beta = -2$ there is a significant reverse flow ($u_{z,max}^* = -2$). In this section S_A, the measured velocity profile for $\beta = 0$ matches the one of a concentric annulus, while this does not happen for $\beta = -1, -2$. However, in section S_B the experimental measurements match the velocity profiles in concentric annulus for all the cases: $\beta = 0, -1, -2$ at this low Reynolds number.

As before, in order to study the influence of the Reynolds number and n, three experiments have been carried out at $\beta = -2$ and $Re_b \in [4.1, 31]$ and $n \in [0.66, 0.89]$. The results of the numerical model (concentric annulus), for fluids with different pseudoplastic behaviour, show very similar velocity profiles in all three cases, and almost no influence of n. The latter is due to the low velocity gradients in the flow. However, this will not necessarily happen in the pipe with the insert device, where the velocity gradients
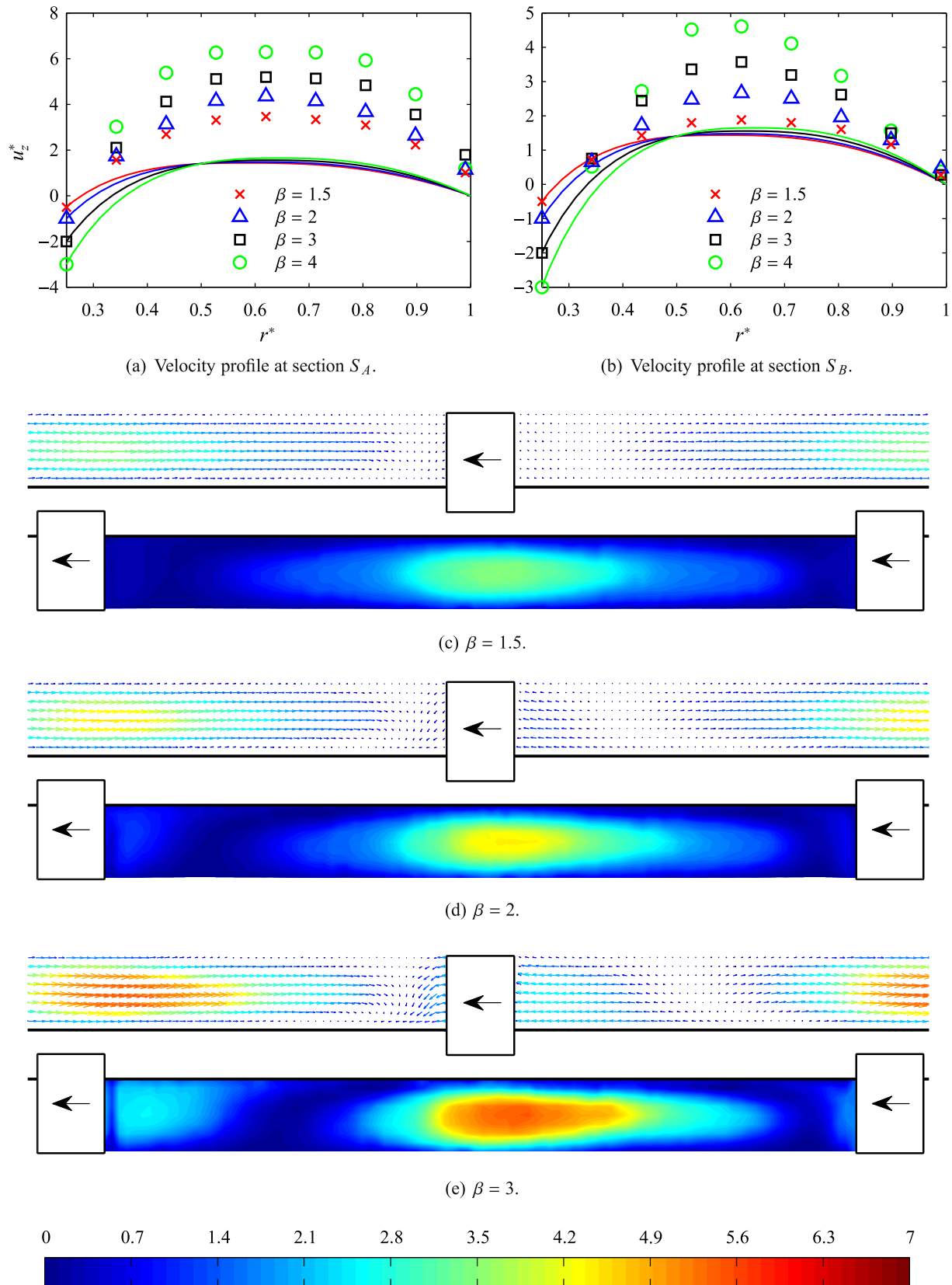
are higher. The experimental results in Fig. 17 show that, when increasing Re_b and n:

- The maximum velocities increase significantly. From values of $u_{z,max}^* = 3$ for the lowest Reynolds ($Re_b = 4.1, n = 0.63$) to a value of $u_{z,max}^* = 5$ for the highest ($Re_b = 31, n = 0.87$).
- For the experiment with higher Re and n, the velocity profile in section S_A (Fig. 17(a)), opposite the scraper position, shows smaller velocities than the other experiments in counter-current direction. The reason is that the reverse flow area has moved upstream.
- In section S_B, the velocity profile for the experiment with the lowest Reynolds number $Re_b = 4.1$, matches the one in a concentric annulus, however if Re_b and n increase, so do the velocities, as this section becomes influenced by the co-current flow generated upstream of the scraper.

5. Conclusions

1. By means of PIV, the flow pattern in the tubular enhanced heat exchanger has been obtained for different scraping velocities, rheological properties of the flow and Reynolds numbers in the laminar region.
2. A numerical model has been created to simulate the flow of pseudoplastic fluids in a concentric annulus. This model has been used to both evaluate the influence of the scraper in the flow pattern, and the importance of the pseudoplastic behaviour of the flow.
3. The *blockage of the flow* parameter has been found to have the highest influence on the flow structure in the ranges under study. In general, if $|\beta|$ is high, there are stronger velocity gradients, recirculation and higher mass transfer from the outer part of the flow to its core. This should lead to heat transfer enhancements as it was by found by Solano et al. [18] for Newtonian fluids. Depending on the value of β, three different flow structures have been detected:
   (a) The first case is when the scraper moves in the same direction but with a velocity higher than the bulk velocity $\beta < 0$. In this case the influence of the scraper on the flow is minimal, and the flow pattern in the laminar region depends entirely on the pseudoplasticity of the fluid.
   (b) In the second case the scraper moves in co-current direction at the bulk velocity $\beta = 0$, then the flow pattern is influenced by the drag effect of the scrapers in the flow.
   (c) For the other cases, where the scrapers block the flow. This can happen in co-current direction if the scraper moves slower than the bulk velocity, if the scraper is static or in the counter-current movement of the scraper. For all three cases the flow pattern is similar and characterized by a high velocity region in the position opposite the scraper.
4. By means of experiments at different values of the Reynolds number and the flow behaviour index n, the influence of the variation of these parameters on the flow has been obtained. When Re and n increase, so do the high velocity areas, the recirculation or reverse flows. Consequently, heat transfer is expected to be enhanced in this situation.
5. Due to experimental limitations, no precise measurement of the isolated influence on the flow of n has been possible. However, the use of the numerical model has helped to establish its order of magnitude. The pseudoplastic behaviour of the fluid (represented by n), will not affect the main flow structure or produce strong differences in the flow pattern. However, pressure drop and heat transfer will indeed be affected by the variations in the velocity gradients produced by the pseudoplasticity of the fluid.
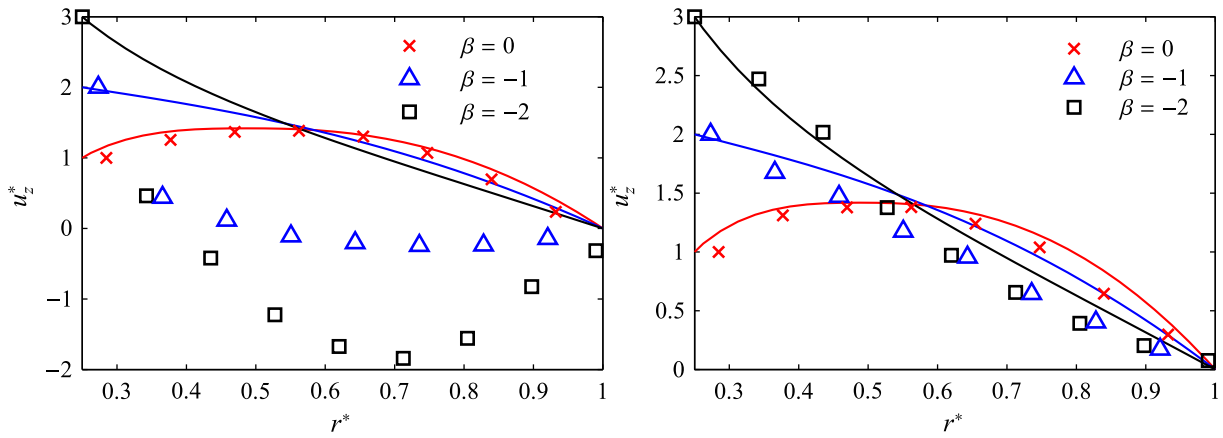
(a) Velocity profile at section S_A.

(b) Velocity profile at section S_B.

(c) $\beta = 1.5$.

(d) $\beta = 2$.

(e) $\beta = 3$.

Fig. 14. Effect of β on the flow pattern for the case of $\beta > 1$. Experiments D-5 to D-8 with $Re_b \approx 4.6, n \approx 0.63$. Representation criteria for "a)" and "b)": *symbols* for pipe with scraping device (experimental results) and *lines* for concentric annulus geometry (numerical results).
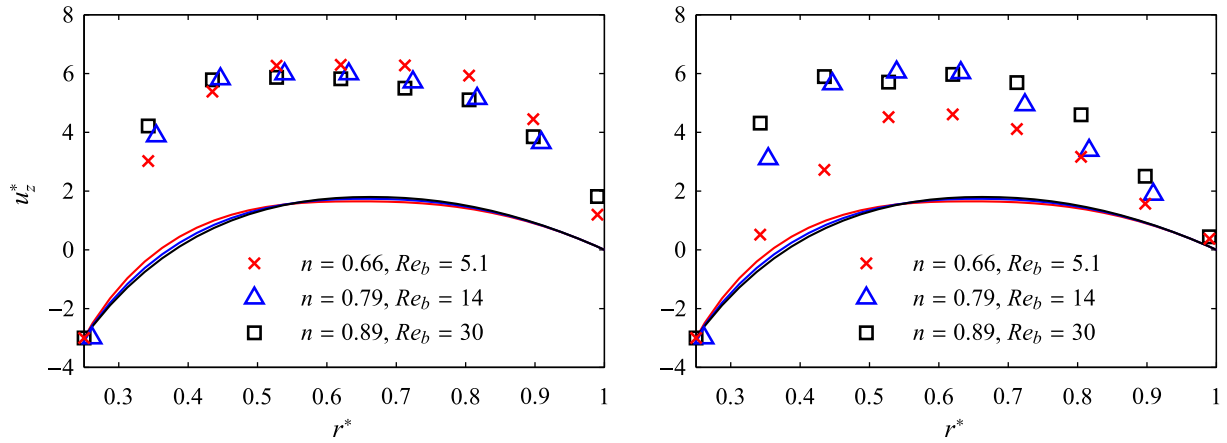
(a) $\beta = 4$. Velocity profile at section S_A at $z = (P - t)/2$.

(b) $\beta = 4$. Velocity profile at section S_B at $z = 3(P - t)/4$.
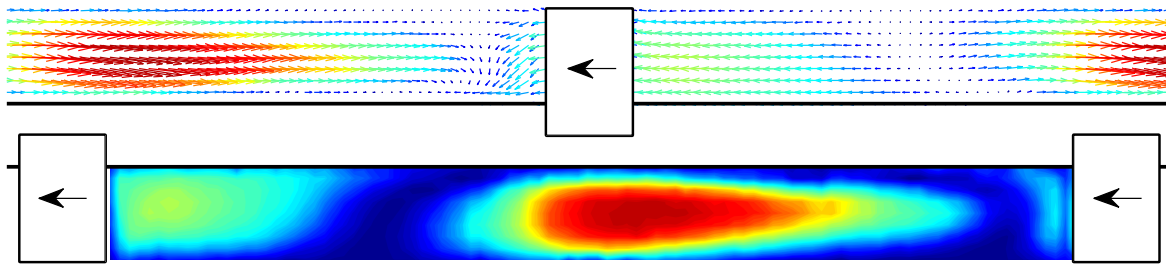
(c) $Re_b = 5.1$, $n = 0.66$.
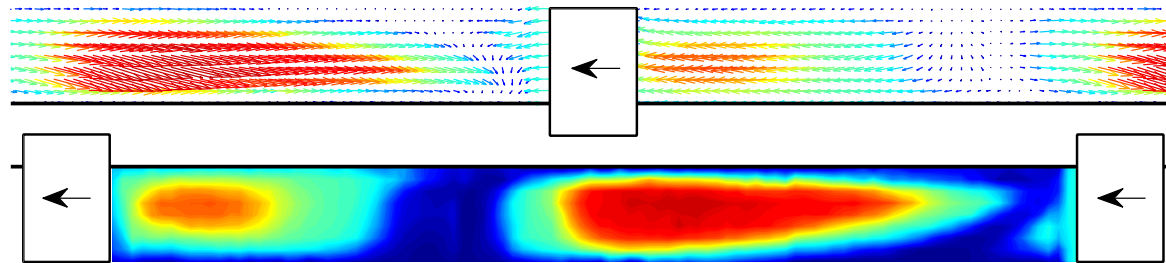
(d) $Re_b = 14$, $n = 0.79$.
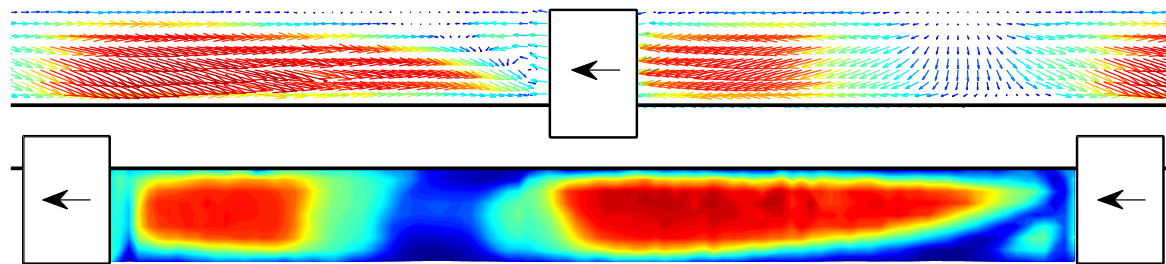
(e) $Re_b = 30$, $n = 0.89$.
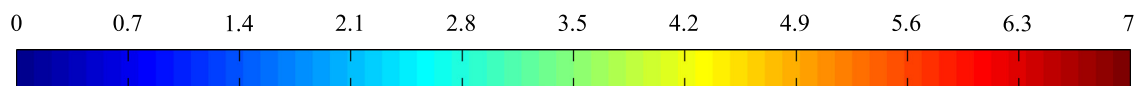
Fig. 15. Effect of Re_b and n on the flow pattern for the case of $\beta = 4$. Experiments D-8, D-12 and D-24. Representation criteria for "a)" and "b)": *symbols* for pipe with scraping device (experimental results) and *lines* for concentric annulus geometry (numerical results).

(a) Velocity profile at section S_A (at $z = (P - t)/2$).

(b) Velocity profile at section S_B (at $z = 3(P - t)/4$).
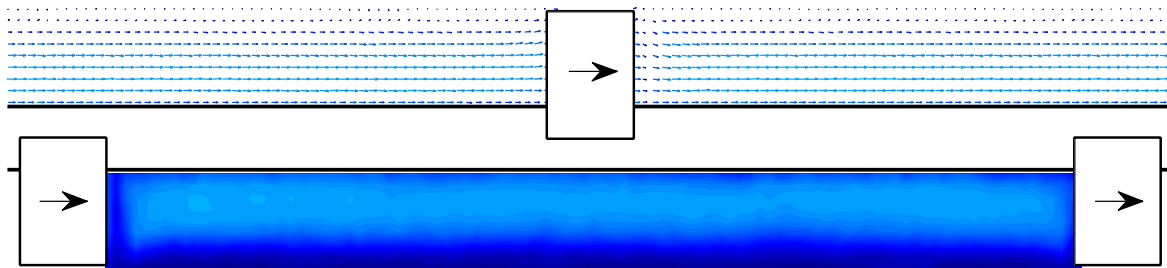
(c) $\beta = 0$.
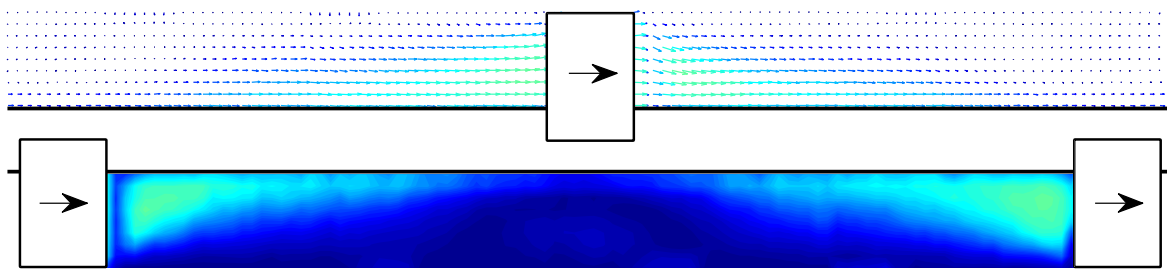
(d) $\beta = -1$.
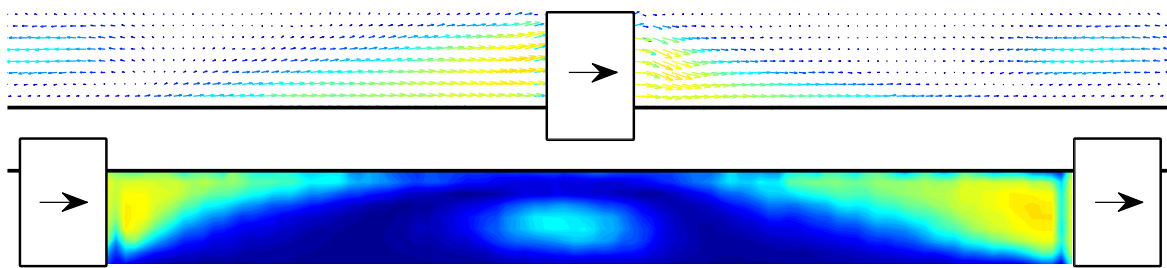
(e) $\beta = -2$.
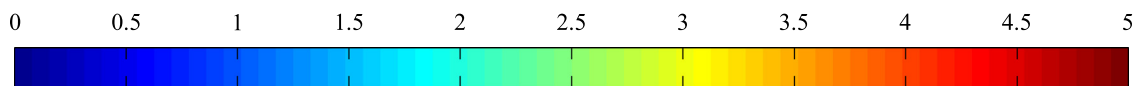
Fig. 16. Flow field for $\beta < 0$, effect of β. Experiments D-2 to D-4 with $Re_b \approx 4.5, n \approx 0.63$. Representation criteria for "a)" and "b)": *symbols* for pipe with scraping device (experimental results) and *lines* for concentric annulus geometry (numerical results).
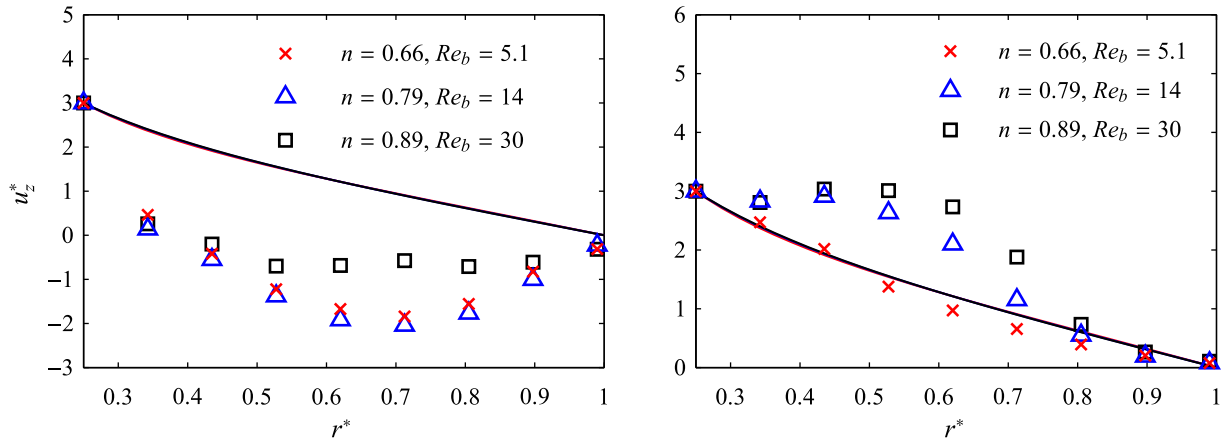
(a) Velocity profile at section S_A (at $z = (P - t)/2$).

(b) Velocity profile at section S_B (at $z = 3(P - t)/4$).
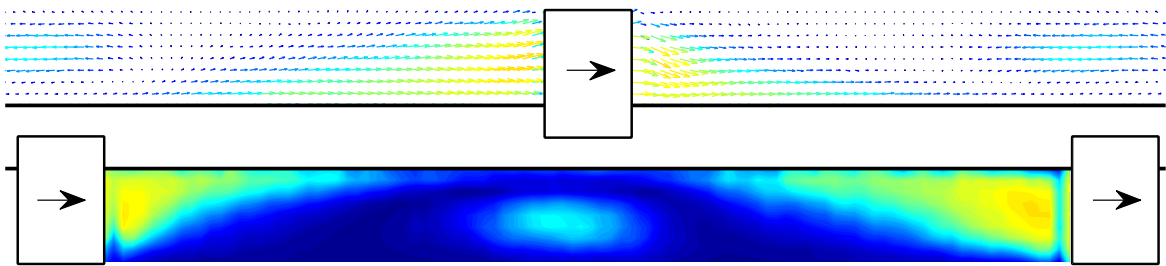
(c) $Re_b = 4.1$, $n = 0.63$.
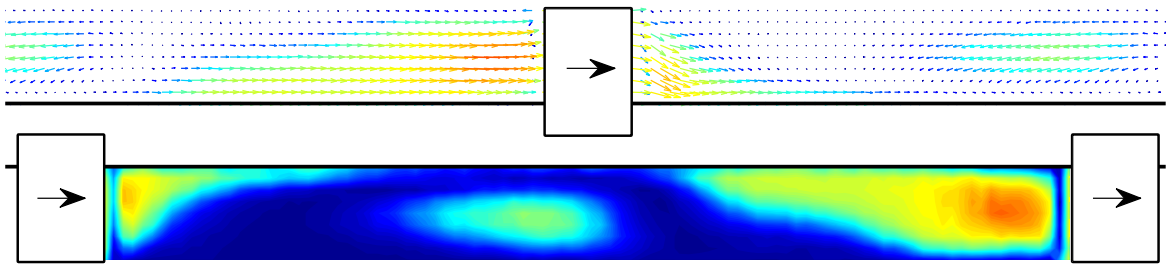
(d) $Re_b = 14$, $n = 0.79$.
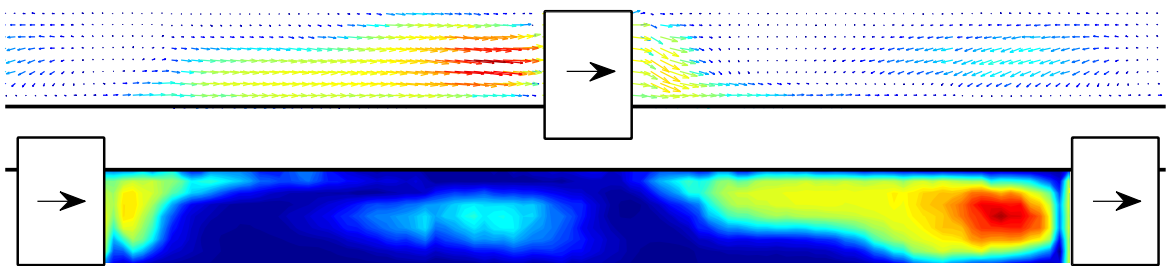
(e) $Re_b = 31$, $n = 0.87$.
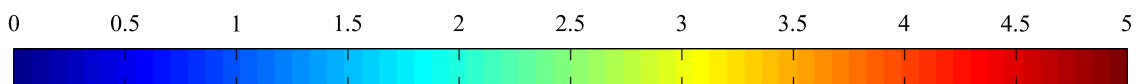
Fig. 17. Flow field for $\beta = -2$, effect of Re_b and n. Experiments D-4, D-16 and D-20. Representation criteria for "a)" and "b)": *symbols* for pipe with scraping device (experimental results) and *lines* for concentric annulus geometry (numerical results).

6. Because of the similarity of the flow structures for the cases with positive *blockage of the flow*, the generalization method developed for static conditions of the scraper is potentially valid for dynamic conditions if the *blockage of the flow* is positive for the full working cycle. This happens if the scraping velocity is low $|v_s| < u_b$.

Acknowledgements

References

[1] K.A. Abdelrahim, H.S. Ramaswamy, High temperature/pressure rheology of carboxymethyl cellulose (CMC), Food Res. Int. 28 (1995) 285–290.

[2] B. Abu-Jdayil, Modelling the time-dependent rheological behavior of semisolid foodstuffs, J. Food Eng. 57 (2003) 97–102.

[3] A. Bergles, Exhft for fourth generation heat transfer technology, Exp. Therm. Fluid Sci. 26 (2002) 335–344.

[4] M. Beuf, G. Rizzo, J. Leuliet, H. Müller-Steinhagen, A. Karabelas, S. Yiantsios, T. Benezech, Fouling and cleaning of modified stainless steel plate heat exchangers processing milk products, in: Heat Exchanger Fouling and Cleaning: Fundamentals and Applications, 2003.

[5] W. Blel, P. Legentilhomme, T. Bénézech, F. Fayolle, Cleanability study of a scraped surface heat exchanger, Food Bioprod. Process. 91 (2013) 95–102.

[6] K.V.K. Boodhoo, L. Smith, J.P. Solano, M. Gronnow, J. Clark, Continuous flow characterization of solid biomass in a reciprocating/rotating scraper tube: an experimental study, AIChE J. 60 (2014) 3732–3738.

[7] M. Cancela, E. Alvarez, R. Maceiras, Effects of temperature and concentration on carboxymethylcellulose with sucrose rheology, J. Food Eng. 71 (2005) 419–424.

[8] R. Chhabra, J. Richardson, Non Newtonian flow and applied rheology, Engineering Applications, Butterworth-Heinemann, 225 Wildwood Av., Woburn, 2008.

[9] D. Crespí-Llorens, P. Martínez, P. Vicente, A. Viedma, Effect of the axial scraping velocity on enhanced heat exchangers, Int. J. Heat Fluid Flow (2013).

[10] D. Crespí-Llorens, P. Vicente, A. Viedma, Generalized Reynolds number and viscosity definitions for non-newtonian fluid flow in ducts of non-uniform cross-section, Exp. Therm. Fluid Sci. 64 (2015) 125–133.

[11] R. De Goede, E. De Jong, Heat transfer properties of a scraped-surface heat exchanger in the turbulent flow regime, Chem. Eng. Sci. 48 (1993) 1393–1404.

[12] M.T. Ghannam, M.N. Esmail, Rheological properties of carboxymethyl cellulose, J. Appl. Polym. Sci. 64 (1996) 289–301.

[13] R. Hanks, K. Larsen, The flow of power-law non-Newtonian fluids in concentric annuli, Ind. Eng. Chem. Fundam. 18 (1979) 33–35.

[14] W. Kozicki, C.H. Chou, C. Tiu, Non-newtonian flow in ducts of arbitrary cross-sectional shape, Chem. Eng. Sci. 21 (1966) 665–679.

[15] M. Raffel, C. Willer, J. Kompenhans, Particle Image Velocimetry: A Practical Guide, Springer, 2000.

[16] J.P. Solano, A. García, P.G. Vicente, A. Viedma, Flow field and heat transfer investigation in tubes of heat exchangers with motionless scrapers, Appl. Therm. Eng. 31 (2011) 2013–2024.

[17] J.P. Solano, A. García, P.G. Vicente, A. Viedma, Flow pattern assessment in tubes of reciprocating scraped surface heat exchangers, Int. J. Therm. Sci. 50 (2011) 803–815.

[18] J.P. Solano, A. García, P.G. Vicente, A. Viedma, Performance evaluation of a zero-fouling reciprocating scraped-surface heat exchanger, Heat Transfer Eng. 32 (2011) 331–338.

[19] K. Sun, D. Pyle, A. Fitt, C. Please, M. Baines, N. Hall-Taylor, Numerical study of 2D heat transfer in a scraped surface heat exchanger, Comput. Fluids 33 (2004) 869–880.

[20] W. Wang, J. Walton, K. McCarthy, Flow profiles of power law fluids in scraped surface heat exchanger geometry using MRI, J. Food Process. Eng. 22 (1999) 11–27.

[21] R.L. Webb, Principles of Enhanced Heat Transfer, Wiley Interscience, 2005.

[22] X.H. Yang, W.L. Zhu, Viscosity properties of sodium carboxymethylcellulose solutions, Cellulose (2007).